FPGA BASED REALIZATION OF AIC FOR APPLYING CS TO RADAR

X. Chen, Y. Zhang, and X. Zhang

Center for Space Science and Applied Research
CAS, Beijing 100190, China

Abstract—Research on digital modeling and realization of non-correlation measurement frame for compressive sensing (CS) is conducted aiming at applying CS to imaging radar. FPGA based Analogue-to-Information Converter (AIC) is proposed and implemented. Real measurement data from AIC hardware platform and simulation data from AIC software platform are compressed to get range profiles, and the results agree well with what expected. The results show that the noise and synchronization error in real system deteriorate the performance of AIC thus CS remarkably.

1. INTRODUCTION

The synthetic aperture radar and inverse synthetic aperture radar (SAR/ISAR) can realize long distance high resolution radar imaging at all time and under all-weather conditions, so, they have been widely used in both military and civil applications [1]. High-resolution SAR/ISAR imaging usually requires large bandwidth signal to achieve, and high-speed data sampling and data processing are unavoidable according to Shannon/Nyquist sampling theorem, so it also makes signal acquisition and processing become more and more difficult. The recently proposed compressive sensing (CS) theory states that much lower than Shannon/Nyquist sampling can be realized in signal measurement if the signal is of some sparsity, and it can be accurately reconstructed by resolving a kind of optimization problem [2, 3]. Once CS emerges, it attracts extensive attentions in signal processing, radar, and many other communities. Up to now, lots of works on CS theory and its applications in radar have been conducted [4–19], and some

of them are briefly summarized as follows. Baraniuk and Steeghs applied CS to SAR imaging with pseudo-noise sequence as transmitted signal [4]. Herman and Strohmer addressed resolution issue of CS based radar in point of view of time-frequency analysis and showed that CS radar is of advantage on better resolution over classic radar [5, 6]. Tello et al. introduced a novel Strategy for SAR imaging based on CS and tested the proposed method by using ERS SAR raw data [7]. Ender addressed the generic system architectures and implementation considerations for applying CS, CS based ISAR imaging of satellite was processed using TIRA real data [9]. Gurbuz et al. [10], Yoon and Amin [11, 12] and Huang et al. [13] applied CS to ground penetrating radar (GPR) and through-wall-radar-imaging (TWRI). Subotic et al. applied CS to distributed radar waveforms design, showed their impact and constraints in the distributed radar [14]. Yu et al. applied CS to direction of arrival (DOA) estimation for multiple input and multiple output (MIMO) radar [15]. Xie and Zhang applied CS to stepped-frequency chirp signal processing and got high resolution imaging for a moving train [16]. Shi et al. [17] and Jouny [18] applied CS to ultra wide band (UWB) signal detection. Zhang et al. applied CS to ISAR imaging with limited pulses [19].

As CS theory states that non-correlation measurement is the key step in CS applications. In [20–23], non-correlation measurement scheme — Analog to Information Converter (AIC) were proposed for CS. In [20–22] AIC was implemented by adopting high speed analogue circuit, while digital AIC is implemented based on FPGA in this paper, which is the basis of analog circuit AIC in the practical radar application, and at the same time, which also creates a kind of new method of radar data impression, and proposes a kind of test system based on radar echo simulation signal source. In this work, Matlab/Simulink based AIC model is firstly constructed to conduct non-correlation measurement for chirp radar signal, and then the AIC is realized based on FPGA, real AIC output data for point targets is sampled and reconstructed using CS algorithm.

The paper is organized as follows. Section 2 introduces basic theory of CS. Section 3 introduces the implementation scheme of AIC based on FPGA and presents both simulated and real measurement results. Section 4 summarizes the paper in the end.

2. CS THEORY AND APPLICATION IN THE ISAR

2.1. Brief Introduction to CS Theory

CS theory mainly includes the following steps, i.e., sparse signal representation, signal non-correlation measurement and signal reconstruc-

tion. The signal sparsity or compressibility decides the applicability of CS algorithms.

In CS theory, sparse signal $x \in \mathcal{C}^{N \times 1}$ is not directly measured while it can be expressed by linear combination of a set of bases $\psi = [\psi_1, \psi_2, \ldots, \psi_n, \ldots, \psi_N,]^T$ in terms of signal theory, as shown by the following equation:

$$x = \sum_{n=1}^{N} \psi_n \alpha_n = \Psi \alpha \qquad (1)$$

where ψ_n are the bases; N is the number of basis; $\alpha \in C^{N \times 1}$ is the coefficient vector. When signal x has only K non-zero coefficients and K is much smaller than N, x is called K sparsified, and Ψ is called as sparse base or sparse dictionary.

Signal x can be projected into a set of measurement array $\Phi = [\varphi_1, \varphi_2, \ldots, \varphi_m, \ldots, \varphi_M]$, and the measurements can be denoted by $y_m = \langle x, \varphi_m^T \rangle$, or it can be rewritten as a multiplication of a matrix and a vector,

$$y = \Phi x + n \qquad (2)$$

Here, $x \in \mathcal{C}^{N \times 1}$ is a N-element vector; $y \in C^{M \times 1}$ is a M-element vector; $\Phi \in C^{M \times N}$ is a $M \times N$ measurement matrix; $n \in C^{M \times 1}$ is noise vector in the process of measurement. After substituting (1) into (2), we get the following equation:

$$y = \Phi x + n = \Phi \Psi \alpha + n = \Theta \alpha + n \qquad (3)$$

Here, $\Theta = \Phi \Psi \in C^{M \times N}$ is a $M \times N$ matrix; α is K sparse, $K < M < N$; sparse coefficient α may be resolved by the following signal reconstruction method.

Signal reconstruction is the third key issue in CS theory, and it is the most direct reconstruction algorithm to get formula's optimization resolutions by L0 norm method. It can be expressed by

$$\min_{\alpha} \|\alpha\|_{l_0} \quad s.t. \quad y = \Theta \alpha \qquad (4)$$

Here, sparse coefficient α can be estimated by the above optimization approach. Equation (4) cannot directly be resolved because it is NP-hard resolution problem. Donoho and Candes point out that Equation (4) may be changed to l_p-norm optimization problem ($0 < p < 2$) when matrix Θ meets a kind of limitation condition. It is written as

$$\min_{\alpha} \|\alpha\|_{l_p} \quad s.t. \quad \|y - \Theta \alpha\|_2 \le \varepsilon \qquad (5)$$

Sparse coefficients α can be obtained through Equation (5), and measurement matrix Φ needs to meet the Uniform Uncertainty

Principle (UUP). It is defined by

$$C_1 \frac{M}{N} \leq \frac{\|\Phi x\|}{\|x\|} \leq C_2 \frac{M}{N} \tag{6}$$

2.2. Sparsity of Radar Echo Signal

In radar imaging, target can be treated as discrete scattering centers. Let us assume that chirp signal is the transmitted signal, i.e., $s_T(t)$ is:

$$s_T(t) = rect(t/T) \exp(j2\pi f_0 t + j\pi K_r t^2), \quad 0 < t < Tp \tag{7}$$

where f_0 is the carrier frequency; K_r is the chirp rate; and Tp is the pulse width. The corresponding reflected signal from a single target (single scattering center) at distance r can be expressed as:

$$\begin{aligned} s_R(t) &= \sigma rect[(t-\tau)/T] \exp[j2\pi f_0(t-\tau) + j\pi K_r(t-\tau)^2] \\ &= \sigma \exp[j2\pi f_0(t-\tau)] \cdot rect[(t-\tau)/T] \exp[j\pi K_r(t-\tau)^2] \end{aligned} \tag{8}$$

Here, $\tau = 2r/c$ is the delay time, and σ is the reflection coefficient. Reference [25] indicates that when the target's dimension is far smaller than that determined by the time window of data recording, the radar echo may be thought to be sparse and CS theory can be applied to the echo data sampling and signal reconstructing in one-dimension range, because of retaining the echo phase information based on CS algorithm. The next step is to have pre-filter and FFT in the cross-range, and the final ISAR two-dimension image may be generated. Like ISAR imaging process, firstly, compressed radar echo needs be processed according to motion compensation algorithm in the range direction; secondly, echo signal matrix should be processed in cross-range direction.

2.3. Non-correlation Measurement of Radar Signal

Based on the sparsity of radar signal, in the following, how to implement no-correlation measurement is presented, which is one of the key steps as shown in Figure 1 for applying CS to radar imaging. Another key step of CS based radar imaging is the signal reconstruction, which will not be addressed here.
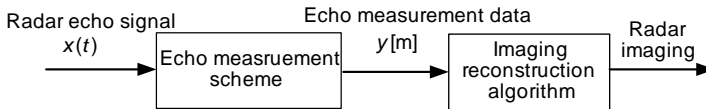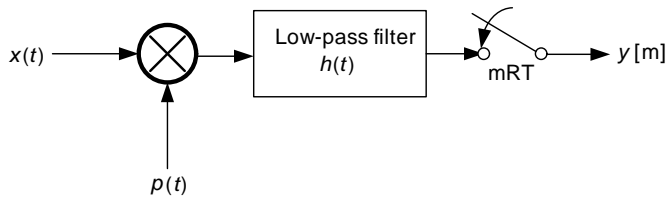

Figure 1. CS based radar imaging algorithm.

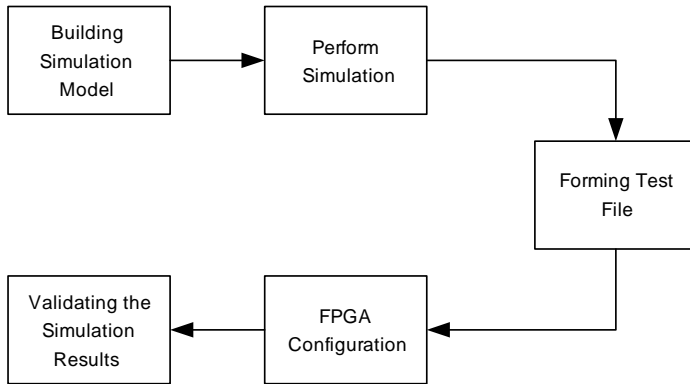**Figure 2.** AIC measurement framework.

Figure 3. Design procedure diagram.

Kirolos et al. proposed an AIC implementation diagram [20] to perform non-correlation measurement on radar signal as shown in Figure 2, where $x(t)$ expresses the echo signal, and $p(t)$ is a high-speed random sequence of non-correlation measurement matrix. According to the AIC scheme, the radar echo signal is firstly randomly sampled with a speed as high as twice of the signal bandwidth, and then the sampled echo data is low-pass filtered and decimated to form a signal which could be digital sampled with much lower rate than that required by Nyquist theorem. In Kirolos's approach, AIC measurement framework was implemented by analogue advices, but here it is implemented digitally based on FPGA.

3. FPGA BASED AIC REALIZATION

3.1. AIC Design Procedure

In this section, we shall introduce briefly the developing platform of FPGA. In our AIC design, Xilinx company's Virtex-4 FPGA is used with XtremeDSP development Kit-IV including Xilinx company's ISE11.1 IDS and Mentor Graphics company's Modelsim simulation

software. Figure 3 outlines the design procedure.

In the design, AIC simulation model is firstly built up by the System Generator in ISE, and then simulation data can be generated in the MATLAB, which is in accord with the data interfacing format. Test file is generated with simulation data so as to perform pre-simulation by using ModelSium. After obtaining correct simulation, FPGA hardware configuration file can be formed and downloaded to FPGA developing board to perform real data simulation. Finally, both simulated data and real output data and reconstruction results are compared and validated.

3.2. Simulation Model of AIC

In this section, AIC simulation model shall be constructed in System Generator, which is seamlessly connected to Matlab/SimuLink and can be started in standard Matlab toolbox. Different modules of Xilinx library can be used to simulate different algorithms. The constructed simulation diagram is shown in Figure 4.
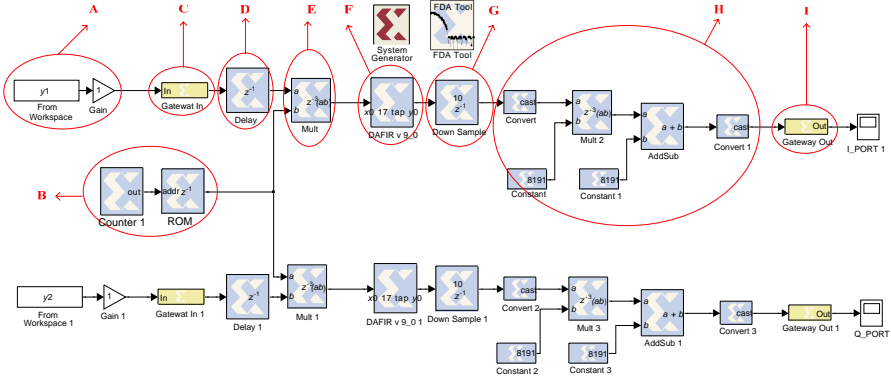

Figure 4. AIC Matlab/Simulink simulation diagram.

In the following, we shall interpret the simulation diagram in detail. In Figure 4, "A" is the module of echo data source from WorkSpace; "B" module generates and stores the random sequence measurement matrix base on CS theory; "C" is the GatewayIn module, which is used for transforming double precision data into 16-bit integer data with 12-bit denoting fractional numbers; "D" is the Delay module used for synchronize the output I data and Q data flowing into the two ports of Multiplexing module E; the Multi module "E" is used to execute the multiplication of radar echo data and random measurement sequence and realize random sampling of radar echo; "F"

is the low-pass FIR filter module; "G" is the Downsample module used for decimating the low-pass filtered data; module "H" truncates and converts the data to make them with the same data format as input of C module; "I" is the GatewayOut module to transform integer data into double precision numbers suitable for D/A.

Now we conduct simulation experiments to test the effectiveness of the diagram. The basic idea is to use simple modulation sequences to modulate echo data from A (completed in E), low-pass filter the modulated output, decimate the filtered output, perform data conversion so as to finally complete the whole simulation. Before experiment, let us assume the following test conditions: (1) Chirp is used as the transmitted signal and the echoes have been transformed into the 16-bit integer numbers; (2) two modulation sequences are chosen (generated and stored in B), i.e., constant sequence of $\{1\,1\,1\,\ldots\,1\,1\,1\}$ and the period sequence of $\{1-1\,1-1\,\ldots\,1-1\,1-1\}$, these sequences are the test vector signal of AIC module for the
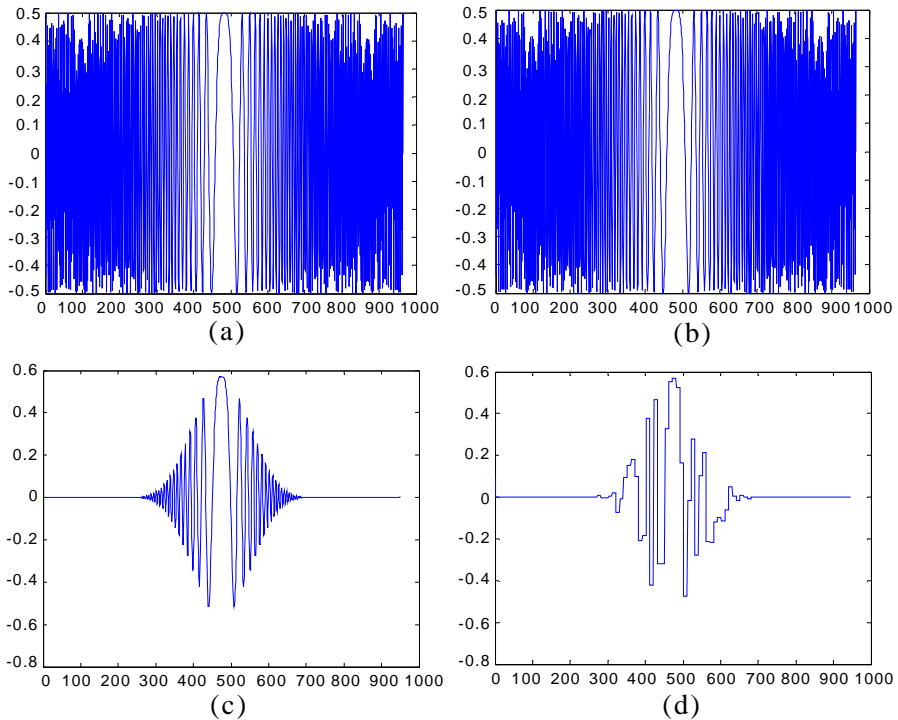

Figure 5. Simulation results by using the sequence of $\{1\,1\,1\,\ldots\,1\,1\,1\}$. (a) Original I component of chirp signal, (b) multiplied signal, (c) low-pass filtered signal, (d) decimated signal.
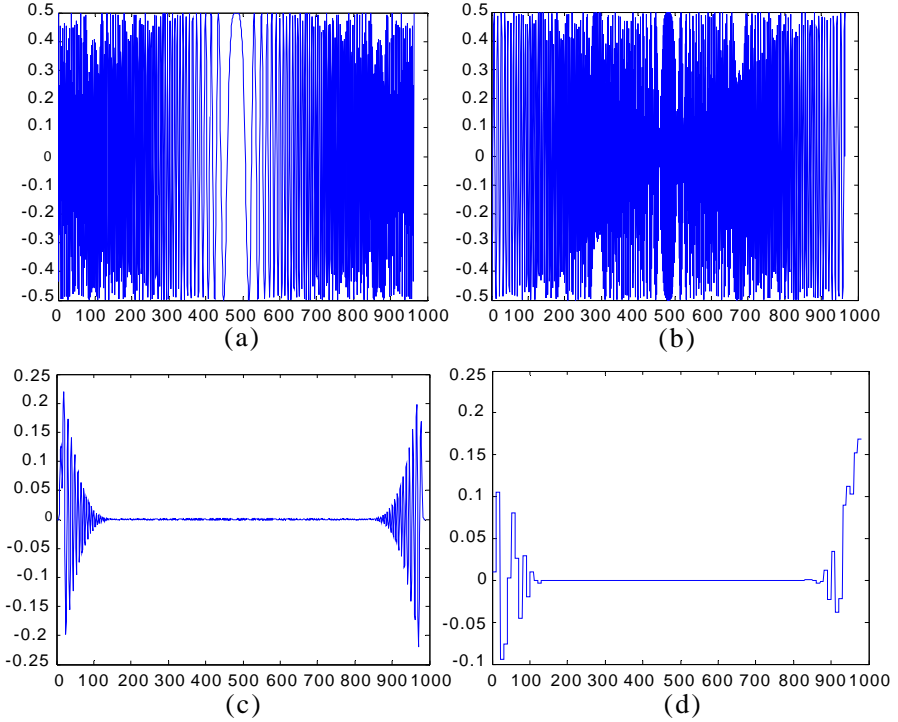
Figure 6. Simulation results by using the period sequence of $\{1 - 1\ 1 - 1 \ldots 1 - 1\ 1 - 1\}$. (a) Original I component of chirp signal, (b) multiplied signal, (c) low-pass filtered signal, (d) decimated signal.

validity; (3) the filter is customized by normalization parameters, i.e., band pass frequency $\omega_{pass} = 0.1$, cutoff frequency $\omega_{stop} = 0.4$, pass band amplitude ripple $A_{pass} = 1\,\mathrm{dB}$, stop band amplitude attenuation $A_{stop} = 80\,\mathrm{dB}$. In the following, simulations shall be conducted by using the above two sequences, and the corresponding results are shown in Figures 5 and 6, respectively, where the waveforms at different positions are presented. It is very clear that the shown results of Figures 5(b), (c) and (d) are quite different from those of Figures 6(b), (c) and (d). The reason is the equivalent low-pass filtering effect of constant modulation sequence (CMS) and the equivalent high-pass filtering effect of periodic modulation sequence (PMS). Both of Figures 5 and 6 show that the AIC function is correctly performed. In Section 3.3 we shall implement the simulation diagram into FPGA, obtain the real AIC output waveforms and compare them with the simulated waveforms of Figures 5(c), (d) and Figures 6(c), (d).

3.3. Hardare Implementation and Test of AIC

In this section, we implement the AIC into FPGA hardware and further test it. Figure 7 shows the designed hardware test system, where the AIC module (marked in red) is realized by FPGA. In the test system, main control computer generates the simulated radar echo data, which is then downloaded to the FIFO in FPGA through PCI interface [24]. FIFO not only acts as the data buffer, but also acts as the clock domain convertor. AIC receives the FIFO output data, executes non-correlation measurement and outputs the downsampled digital I/Q waveforms, which meet the interface requirement of D/A convertor, and finally D/A outputs the compressive sensed measurement signal.

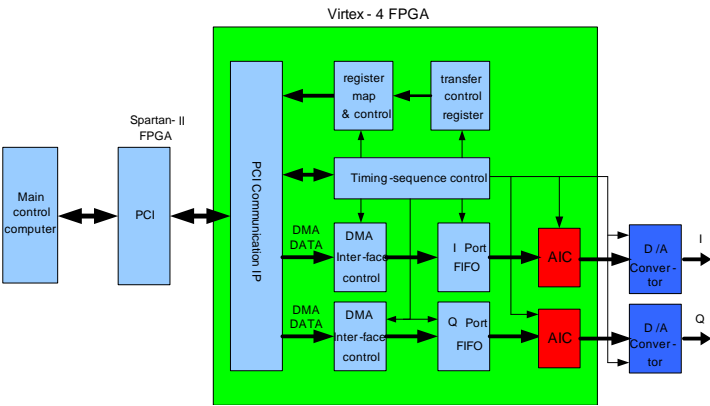Figure 8 shows the real output I/Q waveforms corresponding to

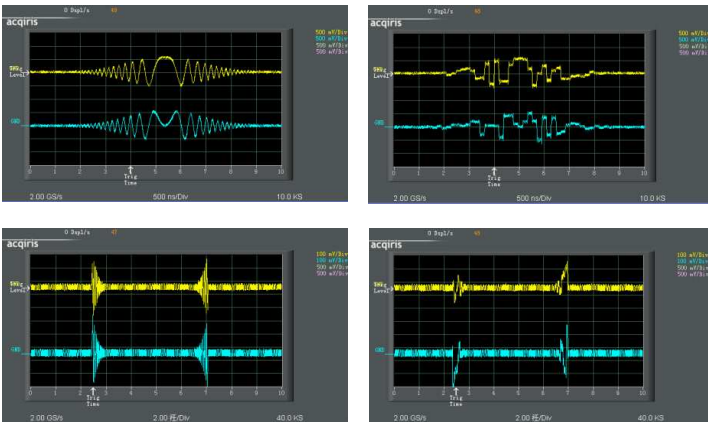**Figure 7.** FPGA based AIC hardware test system.

Figure 8. Recorded output waveforms from AIC by oscilloscope.

CMS and PMS, from which one can see that the upper I waveforms in the upper-left figure and up-right figure are very similar to that from software simulations as shown in Figures 5(c), (d), and the upper I waveforms in lower-left figure and lower-right figure are also very similar to that from simulations as shown in Figures 6(c), (d).

3.4. CS Measurement and Signal Reconstruction

In this section, we present CS measurement and reconstruction results for radar echo of four point targets. The CS measurement is completed by the hardware system shown by Figure 7. Here, pseudo-random modulation sequence (PRMS) is used instead of CMS or PMS. For comparing purpose, we also present the results obtained by software simulation. The used radar parameters are as follows, chirp signal bandwidth B $= 20$ MHz, pulse width $T_p = 14$ µs, data sampling rate $= 50$ MHz. The four targets are positioned at 22 m, 57 m, 133 m and 143 m away from the referenced point with reflection coefficients of 0.9, 1.0, 0.9 and 1.0. In the experiment Agilent Sampling Card (ASC) with 8-bit precision is used. The experiment results are presented in Figure 9, where Figures 9(a) and (c) show the real output waveforms (I components) of echo signal and sparse base, respectively, which are sampled by ASC with only 5 MHz sampling rate. Figure 9(e) shows the reconstructed range profile, from which one can see that the obtained range profile is not as good as one expected. In fact, the reconstruction error is due to the high frequency noise in contained in the sampled data, which is induced by both ASC and real circuit. If we adopt low pass filtering (LPF) to the sampled data, much better results can be expected to achieve. Figures 9(b) and (d) show the low-pass filtered counterparts of Figures (a) and (c). Figure 9(f) shows the reconstructed range profile from waveforms of Figures (b) and (d). Obviously, Figure 9(f) is much better than Figure 9(e) not only in recovered accuracy (positions and amplitudes) but also in signal to noise ratio (SNR).

For further analyzing the influence of real noise in real system, we also present the experiment results by software simulation, and they are shown in Figure 10. Figure 10(a) is the I-component sampled by 5 MHz. Figure 10(b) is the product of (a) and a corresponding pseudo-random sequence, and the sequence can meet application condition based on Equation (6) of CS reconstruction algorithm. Figure 10(c) is the output waveform from a filter. Figure 10(d) is the downsampled waveform of (c). Figure 10(e) is the reconstructed range profile. For comparing purpose, normal result by matched filtering of (a) is also presented in Figure 10(f).

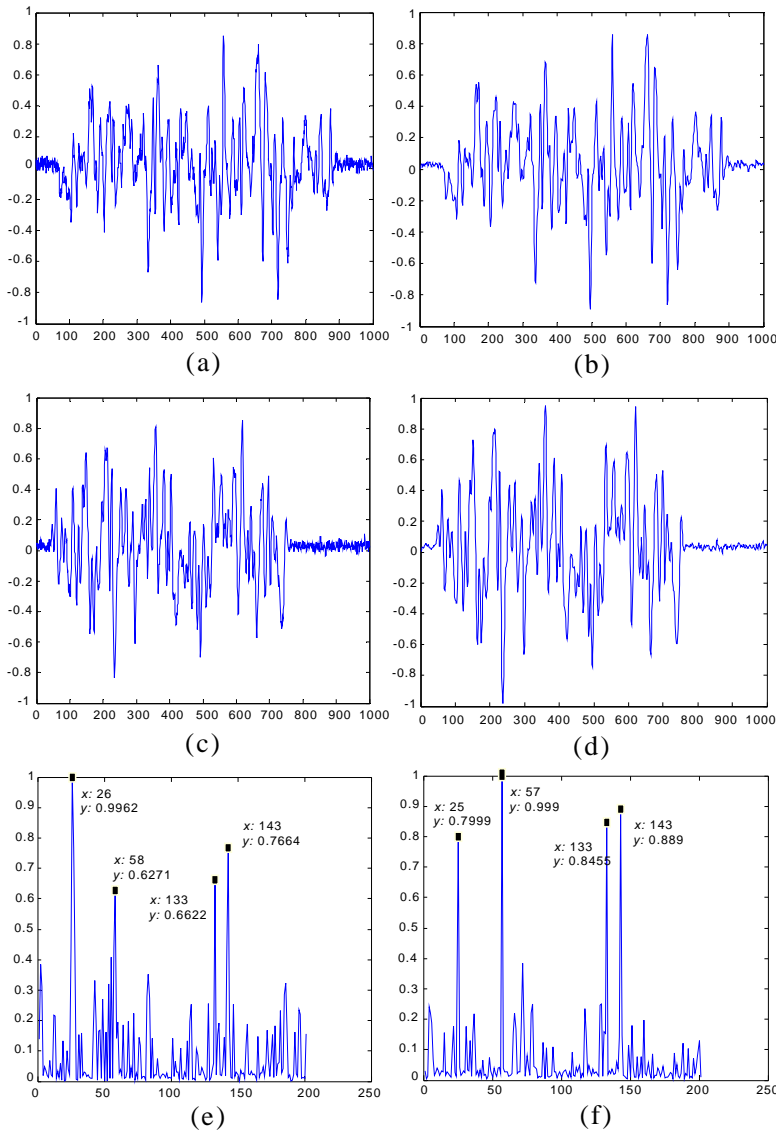In the following, we compare the reconstructed profiles of

Figure 9. CS measurement from hardware and the corresponding reconstructed range profiles. (a) The I-component of echo signal sampled by 5 MHz, (b) the waveform of (a) after LPF, (c) the sparse base sampled by 5 MHz, (d) the waveform of (c) after LPF, (e) the reconstructed range profile without LPF, (f) the reconstructed range profile with LPF.
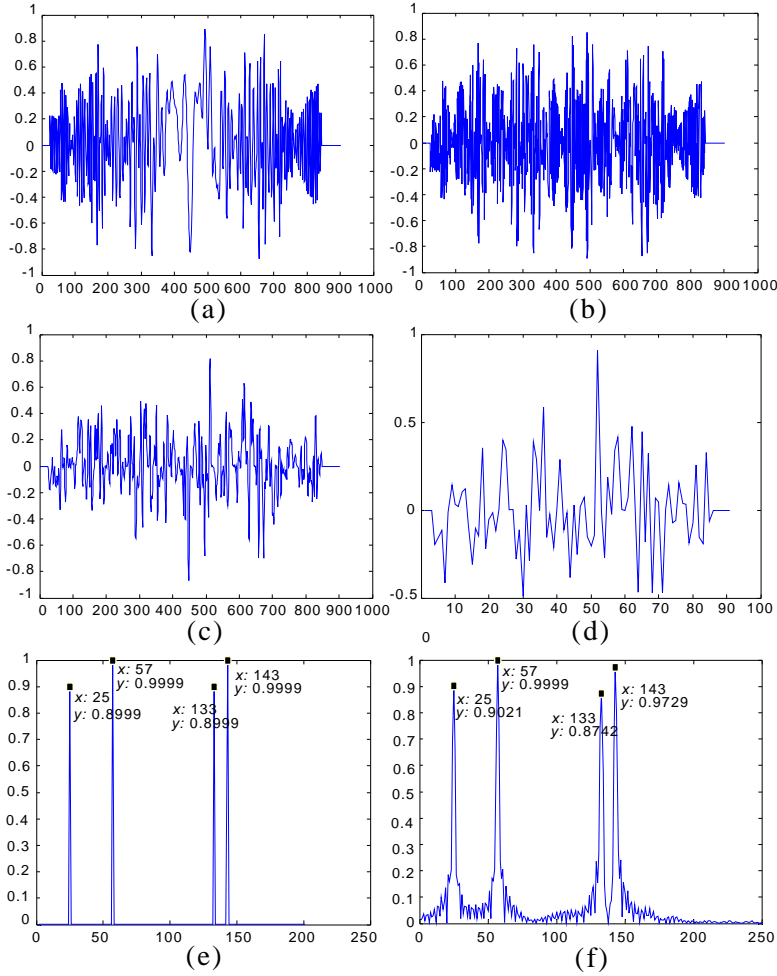
Figure 10. CS measurement from software and the corresponding reconstructed range profiles. (a) The I-component of echo signal sampled by 50 MHz, (b) the product of (a) and a corresponding pseudo-random sequence, (c) low-pass filtered waveform of (b), (d) the downsampled waveform of (c), (e) the reconstructed range profile, (f) the reconstructed range profile by matched filtering.

Figure 9(e), Figure 9(f), Figures 10(e) and 10(f). Figure 10(e) clearly shows the "superresolution" effect compared with Figure 10(f). After comparing Figures 9(e) and 9(f) with Figure 10(e), one can find that this is because the synchronization and noise problem, which is not avoidable in real hardware system, remarkably deteriorate the final reconstruction result. We list the concrete numbers got from the above
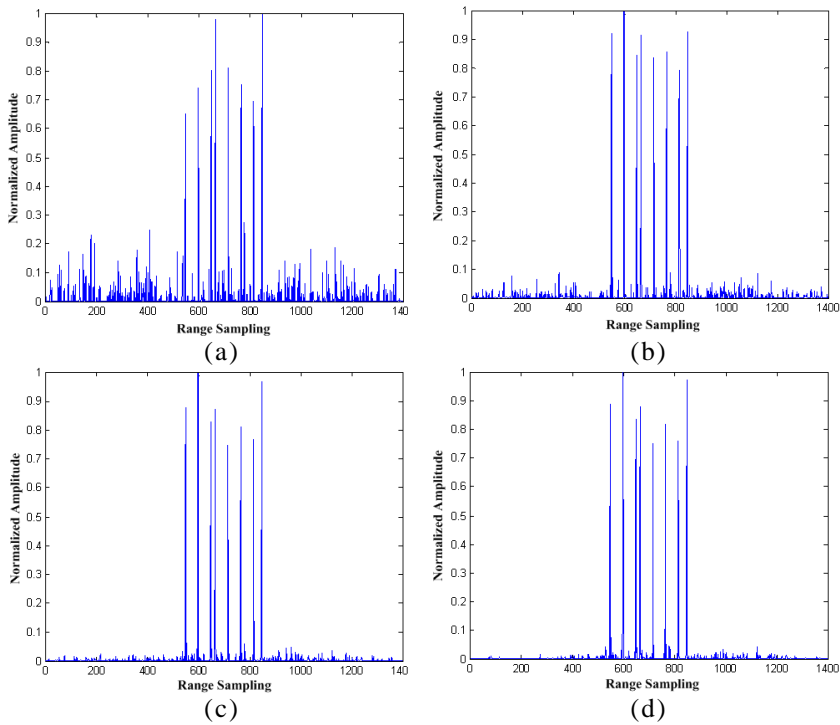
Figure 11. CS reconstructed range profiles from noise-added signals. (a) Reconstructed result when SNR = 10 dB, (b) reconstructed result when SNR = 20 dB, (c) reconstructed result when SNR = 30 dB, (d) reconstructed result when SNR = 40 dB.

four figures in Table 1. In Table 1, case 1, case 2, case 3 and case 4 refer to "CS imaging with data from hardware and without low-pass filtering", "CS imaging with data from hardware and has low-pass filtering performed", "CS imaging with data from software simulation", and "Standard matched-filtering imaging without down sampling on echo". From Table 1, one can see that the software simulated results are most close to the results by normal matched filtering without CS applied. The hardware results without low-pass filtering will lead to big errors in position and amplitude, while with low-pass filter used the reconstruction accuracy can be remarkably improved. In order to compare with the practical measurement, Figure 11 shows different CS reconstructed results from noise-added signals based on the same simulation parameters with Figure 10 except for eight scatter points of target model, and scatter points number is 4 in Figure 9. Here, the added noise is Additive White Gaussian Noise. Four simulation

Table 1. Reconstruction results.

Imaging methods \ Targets	1 (Position, Amplitude) 25 (m) 0.9	2 (Position, Amplitude) 57 (m) 1.0
Case 1	(26, 0.9982)	(58, 0.6271)
Case 2	(25, 0.7999)	(57, 0.9990)
Case 3	(25, 0.8999)	(57, 0.9999)
Case 4	(25, 0.9021)	(57, 0.9999)
Imaging methods \ Targets	3 (Position, Amplitude) 133 (m) 0.9	4 (Position, Amplitude) 143 (m) 1.0
Case 1	(133, 0.6462)	(143, 0.7664)
Case 2	(133, 0.8455)	(143, 0.8890)
Case 3	(133, 0.8999)	(143, 0.9999)
Case 4	(133, 0.8742)	(143, 0.9729)

results show that reconstruction quality will be degraded when SNR becomes lower and lower. It also illustrates the same noise influence as the practical measurement in Figure 9.

4. CONCLUSIONS

In this work, we firstly build up digitalized AIC simulation platform based on Matlab/Simulink and then implement it into FPGA based hardware platform. The performances of both software platform and hardware platform have been tested by simulating CS based measurement and reconstruction of radar echo from four point targets. Only 1/4 data are sampled by CS compared with that required by Nyquist theorem. Experimental results show that the synchronization error between echo measurement and sparse base measurement and the noise in real system are the major facts influencing the performance of CS imaging. Another important issue, robust reconstruction algorithm, will be addressed later on. Both software and hardware platforms are scheduled for further improving, and much work needs to be done.

REFERENCES

1. Wehner, D. R., *High Resolution Radar*, Artech House, Norwood, MA, 1995

2. Tsaig, Y. and D. L. Donoho, "Extensions of compressed sensing," *Signal Processing*, Vol. 86, No. 3, 549–571, 2006.

3. Candes, E. J., J. Romberg, and T. Tao, "Robust uncertainty principles: Exact signal reconstruction from highly incomplete frequency information," *IEEE Transactions on Information Theory*, Vol. 52, No. 2, 489–509, 2006.

4. Baraniuk, R. and P. Steeghs, "Compressive radar imaging," *IEEE Radar Conference*, 128–133, Boston, MA, USA, Apr. 17–20, 2007.

5. Herman, M. and T. Strohmer, "Compressed sensing radar," *IEEE International Conference on Acoustics, Speech and Signal Processing*, 1509–1512, Las Vegas, NV, Mar. 30–Apr. 4, 2008.

6. Herman, M. A. and T. Strohmer, "High-resolution radar via compressed sensing," *IEEE Trans. on Signal Processing*, Vol. 57, No. 6, 2275–2284, 2009.

7. Tello, M., P. Lopez-Dekker, and J. J. Mallorqui, "A novel strategy for radar imaging based on compressive sensing," *IGARSS (IEEE International Geoscience and Remote Sensing Symposium)*, II-213–II-216, 2008.

8. Patel, V. M., G. R. Easley, D. M. Healy, and R. Chellappa, "Compressed synthetic aperture radar," *IEEE Journal of Selected Topics in Signal Processing*, Vol. 4, No. 2, 244–254, 2009.

9. Ender, J. H. G., "On compressive sensing applied to radar," *Signal Processing*, Vol. 90, 1402–1414, 2010.

10. Gurbuz, A. C., J. H. McClellan, and W. R. Scott, "A compressive sensing data acquisition and imaging method for stepped frequency GPRs," *IEEE Trans. on Signal Processing*, Vol. 57, No. 7, 2640–2650, 2009.

11. Yoon, Y. S. and M. G. Amin, "Compressed sensing technique for high-resolution radar imaging," *Proceedings of the SPIE (the International Society for Optical Engineering)*, Vol. 6968, 69681A-69681A-10, 2008.

12. Yoon, Y.-S. and M. G. Amin, "Imaging of behind the wall targets using wideband beamforming with compressive sensing," *IEEE/SP 15th Workshop on Statistical Signal Processing*, 93–96, 2009.

13. Huang, Q., L. Qu, B. Wu, and G. Fang, "UWB through-wall imaging based on compressive sensing," *IEEE Transactions on Geoscience and Remote Sensing*, Vol. 48, No. 3, 1408–1415, 2009.

14. Subotic, N. S., B. Thelen, K. Cooper, W. Buller, J. Parker, J. Browning, and H. Beyer, "Distributed RADAR waveform design based on compressive sensing considerations," *Radar*

Conference, 1–6, 2008.

15. Yu, Y., A. P. Petropulu, and H. V. Poor, "Compressive sensing for MIMO radar," *ICASSP (IEEE International Conference on Acoustics, Speech, and Signal Processing)*, 3017–3020, 2009.

16. Xie, X. and Y. Zhang, "High-resolution imaging of a moving train by ground-based radar with compressive sensing," *Electronic Letters*, Vol. 46, No. 7, 529–531, Apr. 1, 2010.

17. Shi, G. M., J. Lin, X. Y. Chen, et al., "UWB echo signal detection with ultra-low rate sampling based on compressed sensing," *IEEE Transactions on Circuits and Systems II — Express Briefs*, Vol. 55, No. 4, 379–383, 2008.

18. Jouny, I., "Compressed sensing for UWB radar target signature reconstruction," *Digital Signal Processing Workshop and 5th IEEE Signal Processing Education Workshop*, 714–719, Marco Island, FL, USA, Jan. 4–7, 2009.

19. Zhang, L., M. Xing, C.-W. Qiu, et al., "Achieving higher resolution ISAR imaging with limited pulses via compressed sampling," *IEEE Geoscience and Remote Sensing Letters*, Vol. 6, No. 3, 567–571, 2009.

20. Kirolos, S., T. Ragheb, J. Laska, M. E. Duarte, Y. Massoud, and R. G. Baraniuk, "Practical issues in implementing analog-to-information converters," *The 6th International Workshop on System-on-Chip for Real-Time Applications*, 141–146, 2006.

21. Kirolos, S., J. Laska, M. Wakin, M. Duarte, D. Baron, T. Ragheb, Y. Massoud, and R. Baraniuk, "Analog-to-information conversion via random demodulation," *IEEE Dallas/CAS Workshop on Design, Applications, Integration and Software*, 71–74, 2006.

22. Laska, J. N., S. Kirolos, M. F. Duarte, T. S. Ragheb, R. G. Baraniuk, and Y. Massoud, "Theory and implementation of an analog-to-information converter using random demodulation," *IEEE Int. Symp. on Circuits and Systems*, 1959–1962, New Orleans, LA, USA, May 2007.

23. Fudge, G. L., R. E. Bland, M. A. Chivers, S. Ravindran, J. Haupt, and P. E. Pace, "A Nyquist folding analog-to-information receiver," *42nd Asilomar Conference on Signals, Systems and Computers*, 541–545, 2008.

24. Shanley T. and D. Anderson, *PCI System Architecture*, 4th Edition, MindShare Inc., Toronto, 1999.

25. Xie, X. and Y. Zhang, "2D radar imaging scheme based on compressive sensing technique," *Journal of Electronics & Information Technology*, Vol. 5, No. 32, 1234–1238, 2010.